

Weighted-elastic-wave interferometric imaging of microseismic source location*

Li Lei^{1,2}, Chen Hao^{*1}, and Wang Xiu-Ming¹

Abstract: Knowledge of the locations of seismic sources is critical for microseismic monitoring. Time-window-based elastic wave interferometric imaging and weighted-elastic-wave (WEW) interferometric imaging are proposed and used to locate modeled microseismic sources. The proposed method improves the precision and eliminates artifacts in location profiles. Numerical experiments based on a horizontally layered isotropic medium have shown that the method offers the following advantages: It can deal with low-SNR microseismic data with velocity perturbations as well as relatively sparse receivers and still maintain relatively high precision despite the errors in the velocity model. Furthermore, it is more efficient than conventional traveltimes inversion methods because interferometric imaging does not require traveltimes picking. Numerical results using a 2D fault model have also suggested that the weighted-elastic-wave interferometric imaging can locate multiple sources with higher location precision than the time-reverse imaging method.

Keywords: Microseismic monitoring, seismic source location, elastic wave, interferometric imaging, time-reverse imaging

Introduction

The seismic source location problem is an active research topic in seismology and geophysics. In recent years, as increasingly more low-permeability oil and gas fields are exploited, hydraulic fracturing has become the production method of choice for such oil and gas fields. Monitoring the fracture morphology is critical for the efficiency of fracturing and the subsequent exploration and production. Microseismic monitoring is a geophysical technique that images the location

and distribution of fractures with weak seismic waves induced by hydraulic fracturing or other methods, such as the extraction of oil and gas (Jupe et al., 1998; Liang et al., 2004; Maxwell et al., 2010b; Duncan and Eisner, 2010). Source location is critical for microseismic monitoring.

The basic idea in source location studies is to apply source location inversion using the traveltimes of the seismic waves and a velocity model. Most used methods are linear and are based on the Geiger algorithm (Geiger, 1912), e.g., the P and S or P/S traveltimes difference (Zhang et al., 2002; Song et al., 2008), polarization

Manuscript received by the Editor October 28, 2014; revised manuscript received June 20, 2015.

*This work is supported by the R&D of Key Instruments and Technologies for Deep Resources Prospecting (No. ZDYZ2012-1) and National Natural Science Foundation of China (No. 11374322).

1. State Key Laboratory of Acoustics, Institute of Acoustics, Chinese Academy of Sciences, Beijing 100190, China.

2. University of Chinese Academy of Sciences, Beijing 100049, China.

◆Corresponding author: Chen Hao (Email: chh@mail.ioa.ac.cn)

© 2015 The Editorial Department of **APPLIED GEOPHYSICS**. All rights reserved.

Microseismic source location

analysis, and hodogram method using traveltimes and amplitude data (Maxwell et al., 2010b). Many nonlinear location methods, such as the gradient, Newton, global search, and Monte Carlo methods, have been developed (e.g., Tian and Chen; 2002; Yang et al., 2005). In short, both the theoretical and practical aspects of traveltimes inversion methods have been extensively studied. Mathematically, it is expressed as solving a function of a hypothetical position, which is constructed using the difference between observed and theoretical traveltimes. Methodology improvements lie in the construction of the objective function and solution approaches.

Microseismicity records always involve low signal-to-noise ratio (SNR) data and large datasets. Thus, picking the arrival time in traditional location methods is labor intensive and unreliable, which could affect the location accuracy. Because of the development of microseismicity monitoring technologies, particularly for shale-gas reservoirs, pick-free and automatic location methods have been developed using concepts from reflection seismic exploration. These methods require velocity models to perform wavefield extrapolation or to calculate traveltimes. However, they do not require phase picking, and the full waveform is used to stack and suppress noise in image processing. Therefore, these methods are referred to as imaging or migration-based microseismicity location methods, and they are more adaptive to low-SNR microseismicity than traditional methods.

Imaging methods can be categorized into two types. The first comprises imaging methods based on the time reversal invariance of the wavefield. For example, McMechan (1982) and McMechan et al. (1985) used reverse-time migration to locate three earthquakes in Long Valley, California. Gajewski et al. (2005) verified the energy-focusing method based on the wavefield backward propagation. Artman et al. (2010) proposed a migration-type microseismic event location method based on time-reversed acoustics and imaging conditions. Wang et al. (2013) combined the principle of reverse-time migration with the Wigner distribution function (WDF) and interferometric location algorithm and applied them to three-dimensional (3D) multicomponent seismic records from surface and downhole receiver arrays. Li et al. (2014) also combined reverse-time migration with interferometric imaging and proposed the reverse-time interferometric location algorithm using surface and downhole arrays. The second group of imaging methods is based on the time delay and stacking using the diffraction stacking migration or Kirchhoff migration. For example, Kao et al. (2004, 2007) proposed the

source-scanning algorithm (SSA) to describe the spatial and temporal distribution of the source. Drew et al. (2005, 2013) proposed the coalescence microseismic mapping (CMM) method to obtain a four-dimensional (spatial and temporal dimensions) profile by waveform stacking to increase the SNR of P- and S-waves picked with the STA/LTA algorithm. The CMM method has been successfully integrated to the microseismic monitoring software StimMAP (Burch et al., 2009). Gajewski et al. (2007) and Zhebel et al. (2010) applied diffraction stacking to two-dimensional (2D) and 3D source location. Grigoli et al. (2013, 2014) used SSA to develop an imaging method by stacking STA/LTA-transformed waveforms based on traveltimes. Haldorsen et al. (2012, 2013) proposed a migration-based deconvolution method for microseismic event location and suggested that semblance-weighted (energy-weighted relevance) imaging is superior to the energy correlation imaging proposed by Artman et al. (2010). Miao et al. (2012a, 2012b) proposed a tomographic imaging method to locate microseismic events automatically and invert source parameters in mining industry. Yang et al. (2013) applied seismic emission tomography to microseismic energy inversion in the surface monitoring of the development of tight gas reservoir.

Traditional traveltimes inversion methods involve searching for the location that is most consistent with the traveltimes of recorded waveforms within the target zone, whereas migration-type methods image the source by focusing on the potential energy (amplitude) of grid points. Schuster et al. (2004) pointed out that seismic interferometric imaging can also be used to locate seismic sources, and Grandi et al. (2009) successfully applied it to surface microseismic monitoring of reservoirs.

Seismic interferometry imaging represents an application of seismic interferometry. The latter is a recent seismic exploration method and belongs to a class of processing and imaging methods that are based on correlation or convolution (Schuster, 2009; Wapenaar et al., 2010a, 2010b). The basic principle of the method is based on the reciprocity theorem and the replacement of interferometry data by correlation data. Claerbout (1968) originally studied seismic interferometry and transformed by using auto-correlation the transmission seismogram recorded on the surface of a horizontally layered model to a zero-offset reflection seismogram. Schuster (2001) developed a seismic interferometry method applicable to any type of source–receiver geometries using arbitrary velocity models. Schuster et al. (2004) proposed four cases of seismic interferometry for reflector or source imaging and pointed out that the

main advantage of the method was the ability to image passive seismic data with unknown source location and source wavelet. This is referred to as cross-correlation or interferometric migration because it uses migration and correlation.

In this study, the principle of seismic interferometric migration in the source location is analyzed, and it is pointed out that multiple imaging solutions could be constructed by using cross-correlograms of different wavefields and components. In addition, seismic interferometric imaging method is used for imaging numerically simulated multiwavefield and multicomponent microseismic records of surface and downhole receiver arrays. And a time-window-based weighted-elastic-wave (WEW) interferometric imaging method is proposed, which ensures high precision and eliminates artifacts in the location profile. The effect of noise, receiver spacing, velocity model error, and number of sources on the proposed method is investigated. We compare the WEW interferometric imaging method and time-reverse imaging for multiple sources in a complex fault model, and verify that the proposed method can be used to locate multiple sources.

Basic principles

For microseismic source location, weak seismic signals are recorded by surface or downhole receiver arrays. Then the low-SNR seismograms are used in source parameters inversion. Figure 1 shows a schematic diagram of the microseismic source location problem.

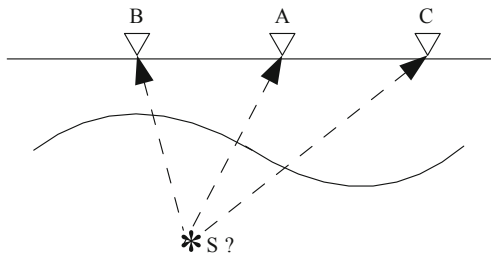


Fig.1 Microseismic source location: ∇ denotes the receiver and $*$ denotes the seismic source.

The basic steps for seismic source location and imaging by interferometric migration are the following. First, we calculate the traveltime by ray tracing or solving the eikonal equation with the given velocity model. Second, seismograms from different receivers are cross-correlated within the selected time window to generate cross-correlograms with traveltime differences.

Third, we conduct interferometric migration to every cross-correlogram and stack all the migration profiles to obtain the final source imaging profile. The migration results for the different wavefields can be stacked if we have the multicomponent data. The equation for the interferometric imaging of the source location is (Schuster et al., 2004; Schuster, 2009)

$$M(x) = \sum_{A,B} \sum_{\omega} \tilde{\phi}(A,B)m(x) = \sum_{A,B} \phi(A,B,t_{Bx} - t_{Ax}), \quad (1)$$

where x is the position of imaging grid point, A and B are two arbitrary receivers, $\tilde{\phi}(A,B)$ and $\phi(A,B)$ are cross-correlation functions of traces A and B in the frequency and time domain, respectively. The interferometric migration kernel function is $m(x) = e^{-i\omega(t_{Bx} - t_{Ax})}$, t_{Ax} and t_{Bx} are the traveltimes of direct waves from imaging point to receivers A and B , respectively, and $t_{Bx} - t_{Ax}$ is the traveltime difference of the direct waves from imaging point to the two receivers. Theoretically, the migration imaging value $M(x)$ is maximum when x is the true source location.

Weighted-elastic-wave interferometric imaging

Either separated single P/S wavefields or elastic wavefields can be used to image the seismic source by interferometric migration. Xiao et al. (2009) separated the elastic wavefield into single P and S wavefields, then, they used interferometric migration in the PP, SS, and PS cross-correlograms and demonstrated that the PS cross-correlation migration profile exhibited better location resolution. The source mechanism of microseisms may include both shear and tension fractures. Thus, most microseismic records include P- and S-waves. Owing to the low SNR of microseismic data, we applied interferometric imaging to the original microseismic elastic wavefields (elastic wave interferometric imaging) to improve the location precision. Since the microseismic data contain both direct P- and S-waves, four types of traveltime differences will be generated in the cross-correlation waveforms of arbitrary receivers A and B

$$\begin{aligned} \Delta t_{AB} &= [(t_A^P - t_B^S), (t_A^P - t_B^P), (t_A^S - t_B^S), (t_A^S - t_B^P)] \\ &= [\Delta t^{PS}, \Delta t^{PP}, \Delta t^{SS}, \Delta t^{SP}], \end{aligned} \quad (2)$$

where t_A^P , t_B^P are traveltimes of direct P-waves of receivers A and B , t_A^S , t_B^S are traveltimes of direct S-waves of receivers A and B , Δt^{PS} is the traveltime difference between the P- and S-waves of the two traces, and Δt^{PP} , Δt^{SS} , and Δt^{SP} have similar meaning. From equations (1) and (2), we know that the elastic wave interferometric

Microseismic source location

imaging does not separate wavefields and makes full use of the microseismic waveforms. The cross-correlation values corresponding to the four types of traveltimes differences are migrated and stacked to image the source. The traveltimes algorithm and velocity model contain errors, the four types of traveltimes differences in equation (2) are replaced by time windows to improve the algorithm stability and reliability, and the equation of time-window-based elastic wave interferometric imaging is

$$M_E(x) = \sum_{A,B} \sum_{\substack{I=P,S \\ J=P,S}} \sum_{n=-w}^w \phi(A, B, t_{Bx}^I - t_{Ax}^J + n\Delta t), \quad (3)$$

where w is the half-length of the time window, Δt is the time step, t_{Bx}^I, t_{Ax}^J ($I, J = P, S$) are traveltimes of different phases (P-wave or S-wave) from imaging point the receivers A and B, respectively, $M(x)$ is the elastic interferometric imaging value. Other symbols have the same meaning as that of equation (1).

In most cases, the S-wave energy of real microseismic data is stronger than that of P-wave energy, we propose to eliminate the small correlation values corresponding to Δt^{PP} , whereas Δt^{PS} , Δt^{PP} , Δt^{SS} values are retained for stacking in the imaging process. It means a weighting coefficient $W = [1, 0, 1, 1]$ is multiplied into the traveltimes differences in equation (2). We define this imaging method as WEW interferometric imaging and the equation is:

$$M_{WEW}(x) = \sum_{A,B} \sum_{\substack{I=P,S \\ J=P,S}} \sum_{n=-w}^w \phi(A, B, t_{Bx}^I - t_{Ax}^J + n\Delta t),$$

when $I = P, J \neq P$. (4)

Numerical experiments

A simple 2D numerical experiment using a horizontally layered isotropic model is conducted to test the performance of the above mentioned interferometric imaging methods. Figure 2 shows the velocity model and source–receiver geometry. The size of the model is 500 m × 500 m and the interfaces are at depths of 100 and 200 m. The P-wave velocities of the different layers from top to bottom are 2000, 2500, and 3000 m/s, respectively, and V_p/V_s is 1.67. The staggered-grid finite-difference method is used to simulate microseismic records (Dong et al., 2000). The simulation parameters are space of 2.5 m, time interval of 0.5 ms, and a 60 Hz ricker wavelet function, which is a horizontally excited force source. Owing to the source size that is much smaller than the fracture length, we use point sources to simulate the microseismic sources (Zhebel and Eisner, 2012). In the two numerical experiments, the source is located at point (250 m, 250 m) and monitored by surface and downhole arrays with 51 geophones. Surface monitoring may be considered for horizontal monitoring wells.

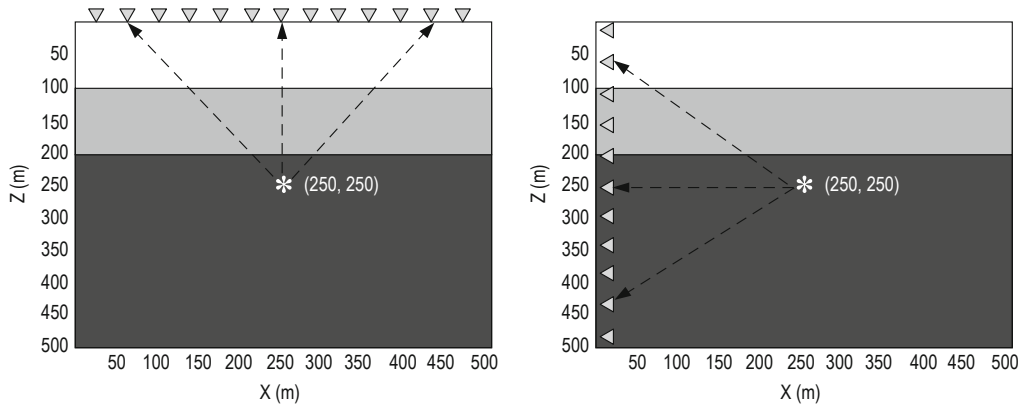


Fig.2 Velocity model, and source–receiver geometry of surface (a) and downhole (b) monitoring.

S-wave, elastic wave and weighted-elastic-wave interferometric imaging methods are used for simulated surface and downhole monitoring. Elastic wavefields are used in the three imaging methods. For S-wave interferometric imaging, only S-wave auto-correlation values are imaged. And the latter two methods image the source with equations (3) and (4), respectively. The

imaging results of V_x and V_z component are stacked to generate the final imaging result. Figure 3 shows 3D views of the normalized interferometric imaging results. The three axes represent the horizontal direction X , depth direction Z , and the normalized square of the image amplitude, respectively.

Figure 3a and 3e suggest that S-wave and elastic wave interferometric imaging yield good location results, whereas, there is an obvious artificial source in the elastic wave interferometric images of surface monitoring (e.g. Figure 3b) owing to disturbances in close P- and S-wave auto-correlation values. The source

cannot be accurately located in S-wave interferometric imaging of downhole arrays (e.g. Figure 3d) because of disturbances in internal multiples. Figures 3c and 3f suggest that the weighted-elastic-wave interferometric imaging can eliminates spurious sources and maintains the precision in surface and downhole monitoring.

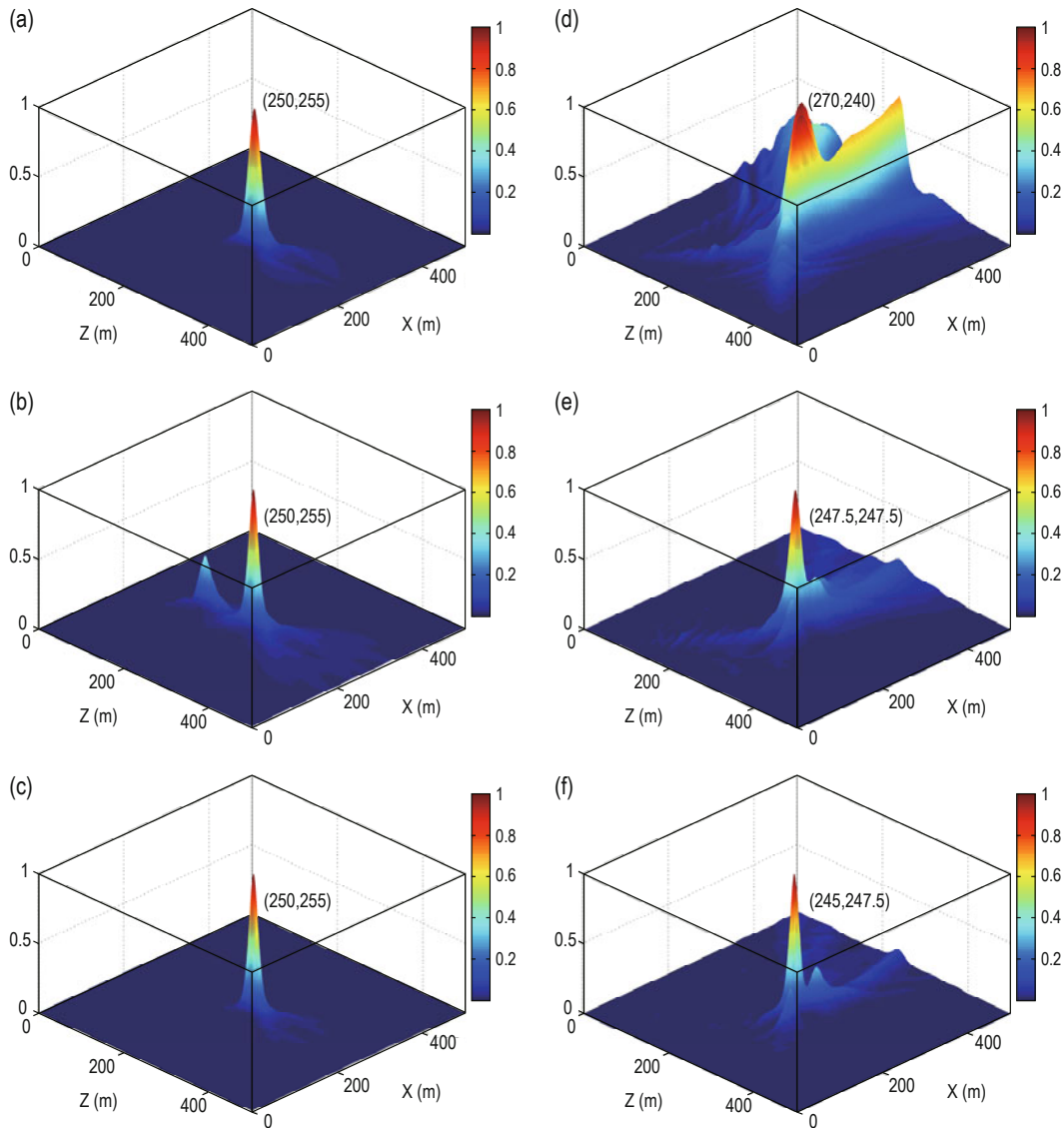


Fig.3 Interferometric imaging results of surface and downhole monitoring.

(a) S-wave interferometric imaging of surface monitoring; (b) Elastic wave interferometric imaging of surface monitoring; (c) WEW interferometric imaging of surface monitoring; (d) S-wave interferometric imaging of downhole monitoring; (e) Elastic wave interferometric imaging of downhole monitoring; (f) WEW interferometric imaging of downhole monitoring

Table 1 lists the interferometric imaging location results for the four of the six cases examined. The feasibility and reliability of the weighted-elastic-wave interferometric imaging was verified for the horizontally

layered isotropic model, and surface and downhole monitoring. The maximum error in the horizontal and vertical direction is ± 5 m, about two grid spacings.

Microseismic source location

Table 1 Interferometric imaging location results

Numerical experiment	S-surface	WEW-surface	E-downhole	WEW-downhole
Source location (m)	(250, 250)	(250, 250)	(250, 250)	(250,250)
Location results (m)	(250, 255)	(250, 255)	(247.5, 247.5)	(245,247.5)
Absolute error (m)	(0, 5)	(0, 5)	(-2.5, -2.5)	(-5, -2.5)

Notes: S-surface: S-wave interferometric imaging of surface monitoring; E-downhole: elastic wave interferometric imaging of downhole monitoring; WEW-surface: weighted-elastic-wave interferometric imaging of surface monitoring; WEW-downhole: weighted-elastic-wave interferometric imaging of downhole monitoring

Figure 4 shows the resolution of the results for the four examined cases. The horizontal and vertical resolution represents normalized imaging amplitudes of all horizontal and vertical positions from the source location. The peak horizontal and vertical resolution values correspond to the horizontal and depth location of the source.

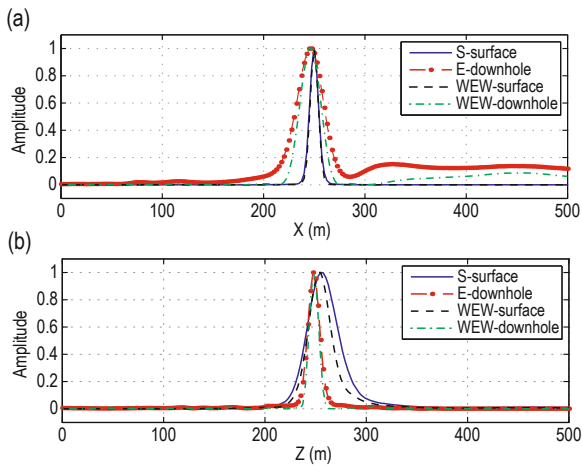


Fig.4 Comparison of the location resolution.

The symbols in the legend is same with symbols meaning in the table 1.

According to Figure 4, the Rayleigh resolution of the location is approximately 10 to 30 m, which is relatively high. The resolution of the locations improves in the horizontal and vertical directions of surface and downhole monitoring, respectively, because the geophone arrays are arranged horizontally and vertically. This means that the horizontal resolution lines of surface monitoring (blue solid line and black dashed line in Figure 4a) and the vertical resolution lines of downhole monitoring (red dot-dashed line and green dotted line in Figure 4b) are sharper near the source position. The weighted-elastic-wave (black dashed and green dot lines) interferometric imaging exhibits better resolution than S-wave and elastic wave interferometric imaging.

Note that the characteristics of the microseismic records vary owing to the unknown source mechanism

and complex subsurface media (Maxwell, 2010a). Although in most cases the S-wave energy is stronger than that of P-wave energy (Das and Zoback, 2013), there are specific situations in which the P-wave energy is equivalent to or stronger than the S-wave energy. To ensure the high precision and resolution of the source location, different imaging resolutions or weighting coefficients are chosen according to the characteristics of the microseismic data. This reflects the flexibility of the seismic interferometry imaging method in locating microseismic sources.

Factors affecting the location precision

To verify the stability and reliability of the weighted-elastic-wave interferometric imaging in locating microseismic sources, factors, such as noise, receiver spacing, velocity model, and number of sources are investigated. Several numerical experiments based on the same horizontally layered isotropic model in Figure 2 are conducted. The simulation parameters are the same as in the previous sections without other specifications.

Noise and heterogeneity

Noise, and errors are added into the simulated seismograms and velocity model. $SNR = 10 * \log_{10}(\bar{S} / \bar{N})$ decreases to 0.01 dB after noise inclusion, where \bar{S} and \bar{N} is the average energy for the signal and noise, respectively. The velocity perturbations are $\pm 5\%$. Figure 5a shows the P-wave velocity after adding random errors and Figure 5b shows the surface records of the Vz component in the noise model. The velocity perturbations and noise are clearly seen. Since a horizontally excited force source is used, the Vz component reaches its minimum in the vertical direction of the source, so the amplitudes of the records right above the source are near zero.

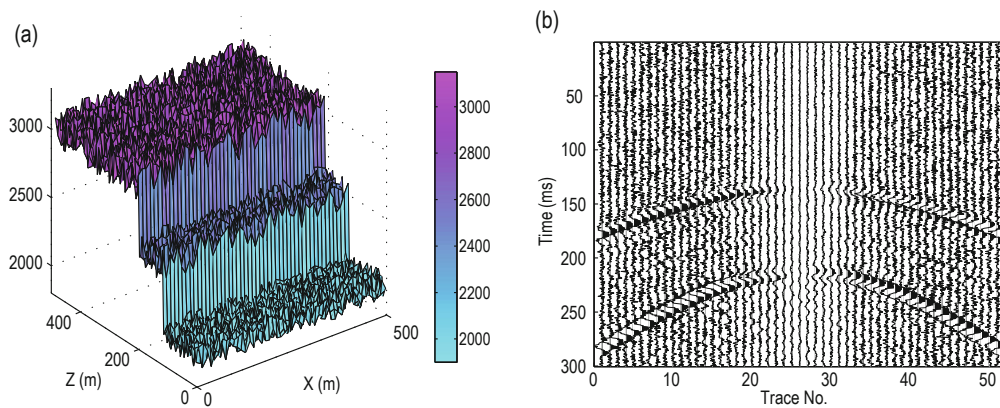


Fig.5 P-wave velocity model (a) and surface record of the V_z component (b).

3D view and profile of the location with the noise model are shown in Figure 6. The weighted-elastic-wave interferometric imaging algorithm shows good

performance even with the noise model. Clearly, the method is stable and reliable.

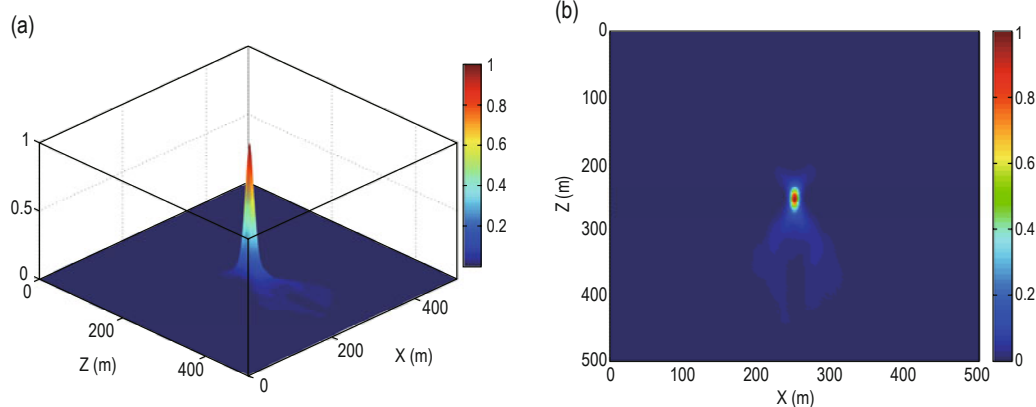


Fig.6 3D view (a) and profile (b) of the weighted-elastic-wave interferometric imaging location with the noise model.

The resolution of the location results of the ideal and noise model in Figure 7 shows that both resolution lines nearly coincide. The weighted-elastic-wave interferometric imaging clearly ensures the high precision and resolution of low-SNR data with velocity perturbations because of the two stacking operations in the cross-correlation and subsequent migration.

Receiver spacing

The initial microseismic monitoring made use of downhole geophone arrays but this is not always possible in practice. Nevertheless, in recent years, surface and near-surface microseismic monitoring techniques have greatly improved. In practical applications, the microseismic data are characterized by low frequency and low noise owing to the distance of the receivers from the source location (Muller, 2013). This is important because it facilitates the development of migration-type location methods.

The numerical experiments in the previous sections

verified that the resolution of the locations is better in the horizontal and vertical directions for surface and downhole monitoring because the imaging process is better constrained in the direction of the receiver arrays. Moreover, the receiver spacing represents the spatial sampling rate, which affects the location indirectly. According to the relation of the sampling rate and spatial alias (Yilmaz, 2001) as well as the parameters in our model, we increase the receiver spacing from 10 to 30 m, 50, 70 to 90 m within the same monitoring space. Figure 8 shows the resolution of the location with different receiver spacings for surface and downhole monitoring. The resolutions of the five receiver spacings are almost identical. Clearly, interferometric imaging can adapt to the relatively sparse receivers because of the effect of stacking in the imaging process. The results suggest that large receiver spacing should be used to maintain the appropriate monitoring space in downhole monitoring. Because of the high cost, only few receivers are used.

Microseismic source location

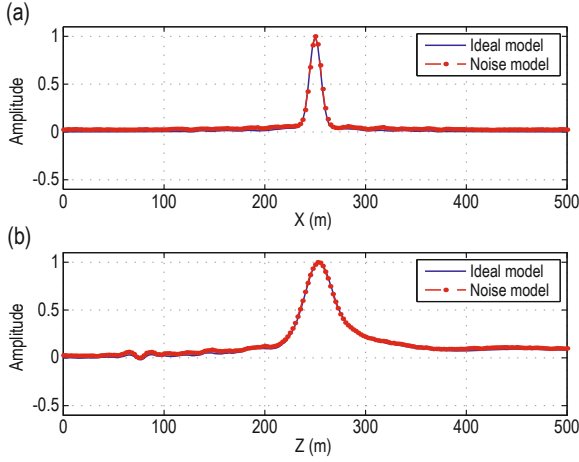


Fig.7 Comparison of the resolution of the locations with the ideal (a) and noise model (b).

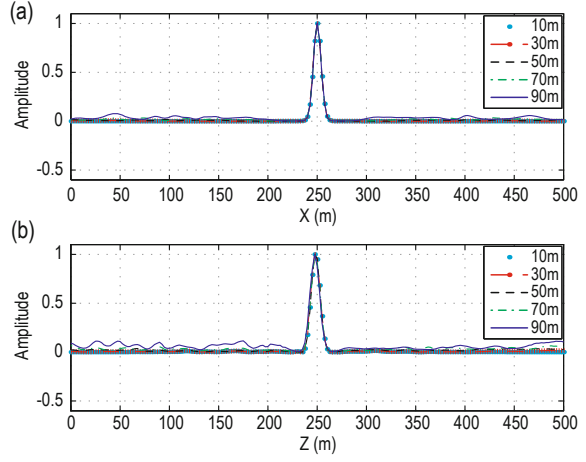


Fig.8 Resolution of the location for different receiver spacings in surface (a) and downhole (b) monitoring.

Velocity model error

The true wave velocity is unknown. Velocity is measured using well logging and perforation data that contain errors; thus, the uncertainties in the velocity model need to be investigated. In the subsequent simulation, we used the surface monitoring model shown in Figure 2a and $\pm 3\%$, $\pm 5\%$, $\pm 8\%$, and $\pm 10\%$ error is added into the model. These velocity models with above errors are used

to calculate traveltimes of direct waves, and the WEW interferometric imaging method is used to image the source. The interferometric imaging uses cross-correlation values that correspond to the traveltimes differences of the different receivers instead of single traveltimes.

Table 2 and Figure 9 show location error vs corresponding velocity error.

Table 2 Location versus velocity model errors

Numerical experiment	Source location (m)	Location results (m)	Absolute error (m)
-10% error	(250, 250)	(250, 282.5)	(0, 32.5)
-8% error		(250, 277.5)	(0, 27.5)
-5% error		(250, 277.5)	(0, 27.5)
-3% error		(250, 255)	(0, 5)
No error		(250, 255)	(0, 5)
+3% error		(250, 255)	(0, 5)
+5% error		(250, 252.5)	(0, 2.5)
+8% error		(250, 235)	(0, -15)
+10% error		(250, 232.5)	(0, -17.5)

$$\Delta t = \frac{l}{\bar{V}_p} - \frac{l}{\bar{V}_p + \Delta \bar{V}} = l \left(\frac{\Delta \bar{V}}{\bar{V}_p (\bar{V}_p + \Delta \bar{V})} \right),$$

$$\Delta T = \left(\frac{l_1}{\bar{V}_p} - \frac{l_1}{\bar{V}_p + \Delta \bar{V}} \right) - \left(\frac{l_2}{\bar{V}_p} - \frac{l_2}{\bar{V}_p + \Delta \bar{V}} \right)$$

$$= \Delta l \left(\frac{\Delta \bar{V}}{\bar{V}_p (\bar{V}_p + \Delta \bar{V})} \right). \quad (5)$$

Figure 9 shows that the WEW interferometric method can accommodate relatively large velocity errors. No effect is seen for $\pm 3\%$ velocity error. When the velocity error increased to $\pm 10\%$, the location error is 20–30 m, which is acceptable in field production. From the relation between traveltimes and velocity variation $|\Delta t| = l \Delta V / (V \pm \Delta V)$ (l is the distance between the source and receiver, V is the average velocity), negative velocity error leads to relatively large traveltimes and location errors. Our results verify this relation.

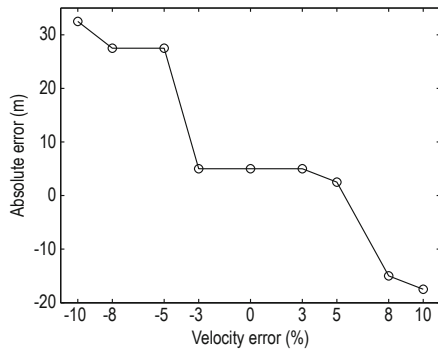


Fig.9 Location error vs velocity error.

Equation (1) suggests that interferometric imaging uses cross-correlation values that correspond to the traveltimes differences of the different receivers instead of single traveltimes. Assuming homogeneous velocity, we obtain the average P-wave velocity \bar{V}_p and velocity error $\Delta\bar{V}$. Then, we calculate the traveltimes error Δt and traveltimes difference error ΔT with the equation (5).

According to the geometric relation, the difference of the source–receiver distance Δl is shorter than the spacing of the receivers, which is typically much shorter than the source–receiver distance l . Clearly, the weighted-elastic-wave interferometric imaging method can tolerate relatively high velocity errors.

Number of sources

There are multiple sources excited simultaneously or continuously along fractures induced by hydraulic fracturing or other engineering operations; therefore, it is important for the proposed method to locate multiple sources. Currently, most location methods is well suited for to locate single microseismic event, but location errors from multiple events hinder the accurate description of the fractures, as well as focal mechanism

inversion (Eisner et al., 2010; Maxwell, 2010a; Li et al., 2013). We conducted two numerical experiments to verify the feasibility of the proposed method in locating multiple sources. The first locates simultaneously excited multiple sources with identical amplitude (Experiment 1). The second locates continuously excited multiple sources with different amplitudes (Experiment 2). Noise and random errors are added into the data and velocity model, respectively, as in the previous sections. Figure 10 shows a schematic diagram of the model and source–receiver geometry. The five sources are (200, 50), (200, 75), (250, 125), (250, 175), and (200, 225).

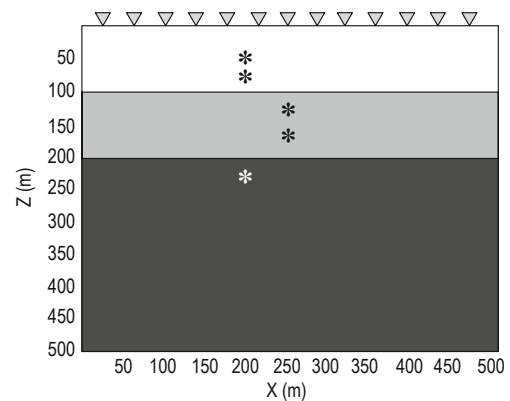


Fig.10 Velocity model and source–receiver geometry of surface monitoring.

Experiment 1 is conducted first. The profile and positive X-axis view of the WEW interferometric imaging results are shown in Figure 11. The results suggest that the resolution decreases as the source–receiver distance increases. Figure 11b shows that the method can locate multiple sources. The normalized imaging amplitude is higher than 0.5 and is strongly related to the true-source amplitude.

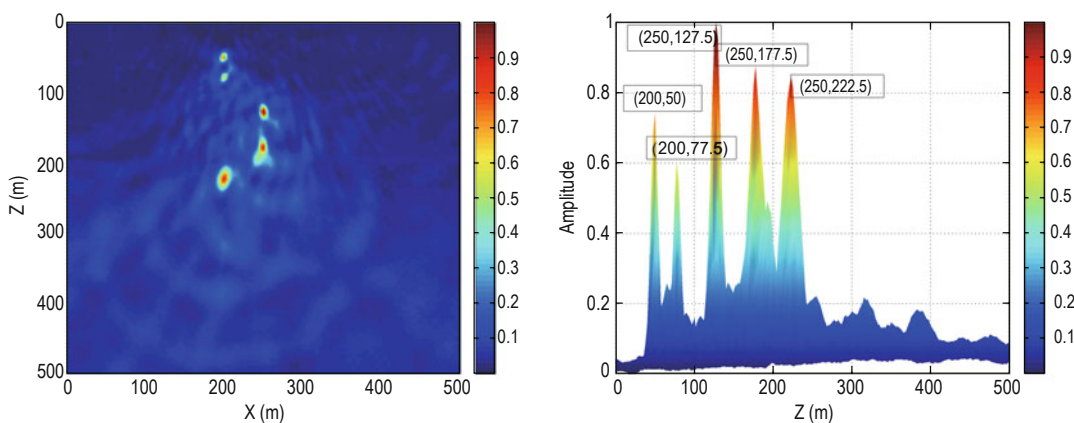


Fig.11 Profile (a) and positive X-axis view (b) of weighted-elastic-wave interferometric imaging results.

Microseismic source location

Figure 12 shows the amplitudes and excitation times of the five sources in experiment 2. The model is the same as in experiment 1, which is shown in Figure 10. The surface microseismic records of the Vz and Vx components are shown in Figure 13. The records of the five events are mixed and overlap, which makes phase picking in the traditional travelt ime inversion methods difficult under such conditions.

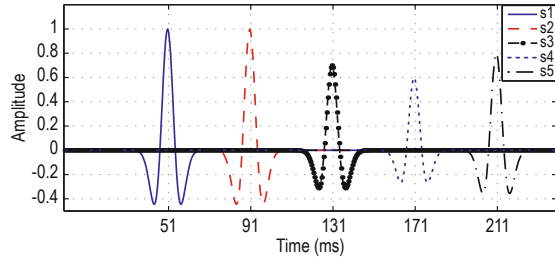


Fig.12 Waveforms of the five sources.

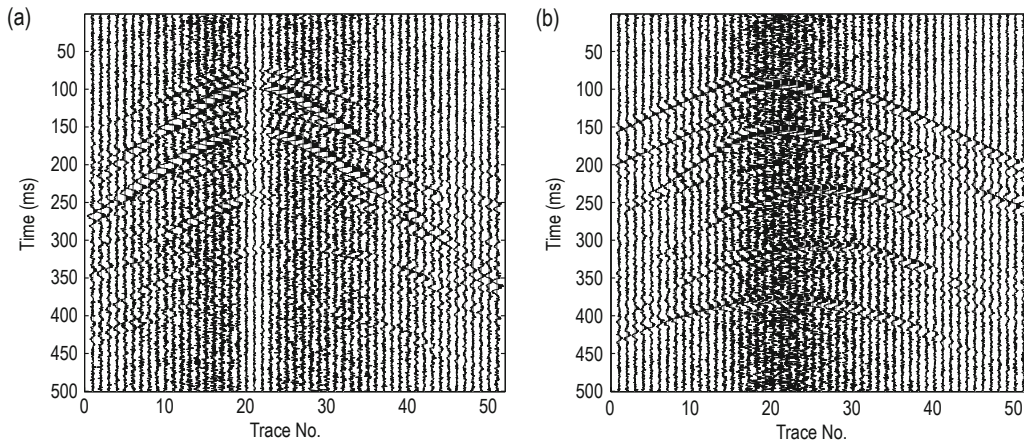


Fig.13 Surface records of the Vz (a) and Vx (b) component.

Figure 14 shows the profile and positive X-axis view of the weighted-elastic-wave interferometric imaging results of experiment 2. The method locates continuously excited multiple sources. The normalized imaging amplitudes of the five sources are shown in Figure 14b

and are consistent with the true amplitudes shown in Figure 12. The two experiments show that preliminary relative amplitudes of the microseismic sources can be obtained with the proposed method.

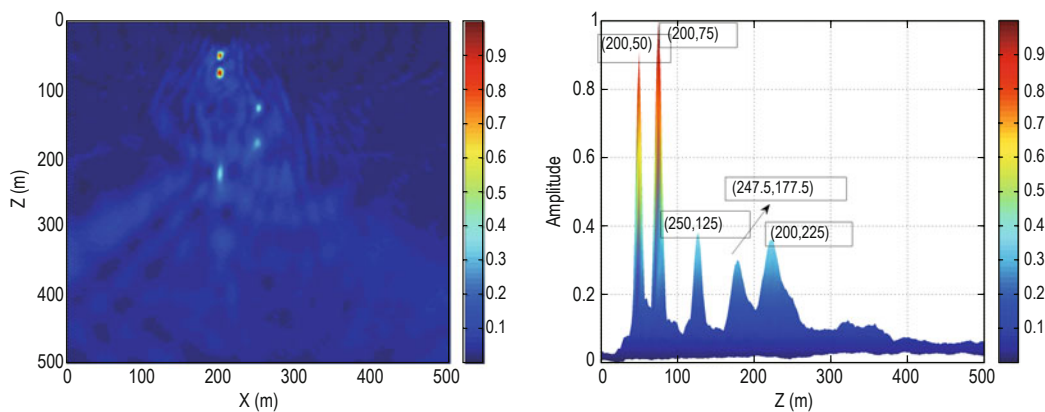


Fig.14 Profile (a) and positive X-axis view (b) of the weighted-elastic-wave interferometric imaging results.

The results of experiments 1 and 2 are given in Table 3. The maximum error of the single direction is 2.5 m (one grid spacing). Because the travelt ime differences of the individual wavefields from different sources are independent, weighted-elastic-wave interferometric

imaging can locate simultaneously or separately excited multiple sources without knowing the excitation time and obtain the relative magnitudes of the different sources as well.

Table 3 Location results

Numerical experiment	Surface monitoring of multiple sources				
Source location (m)	(200,50)	(200,75)	(250,125)	(250,175)	(200,225)
Experiment 1 (m)	(200,50)	(200,77.5)	(250,127.5)	(250,177.5)	(200,222.5)
Absolute error (m)	(0,0)	(0,2.5)	(0,2.5)	(0,2.5)	(0,-2.5)
Experiment 2 (m)	(200,50)	(200,75)	(250,125)	(247.5,177.5)	(200,225)
Absolute error (m)	(0,0)	(0,0)	(0,0)	(-2.5,2.5)	(0,0)

Comparison with time-reverse imaging

We use a 2D fault model extracted from SEG/EAGE salt model (Schuster, 2009) to verify the effectiveness of the proposed method in complex media. Surface monitoring and simultaneously or separately excited multiple sources are used. The location results are compared with those of time-reverse imaging. Figure 15 shows the fault model and the source–receiver geometry. The model consists of six main fault reflections. The P-wave velocity varies between 2500 and 5400 m/s, and there is an apparent low-velocity zone in the middle-right part of the model.

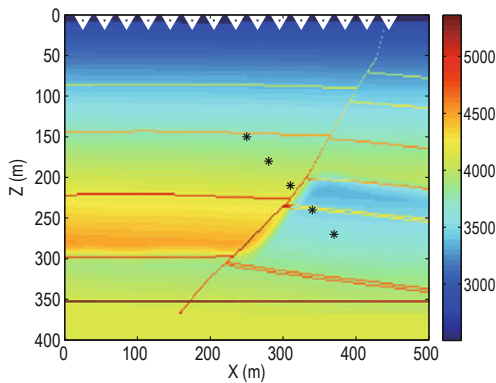


Fig.15 Fault model and source–receiver geometry: ▽ denotes the receiver and * denotes the seismic source.

Time-reversed acoustics (TRA) is a detection method (Fink, 1999) that has been used by seismologists since the early 20th century. The theoretical basis of TRA is the symmetry with respect to the time of the wave equation; namely, the forward wavefield is refocused to the source location along the reverse-time axis. Thus, TRA is also referred to as time-reversal focusing. The wavefield energy is refocused after back propagating the initial wavefield at the excitation time. When the excitation time is unknown in the source location problem, imaging should be used to focus the wavefield. Assume the P- and S-waves are excited simultaneously, they are focused at the source location during the back-propagation process (Artman et al., 2010); therefore, the imaging function will attain maximum zero-lag cross-correlation.

First, we simulate the five simultaneously excited sources using equal amplitudes. The profile of the WEW interferometric and time-reverse imaging results is shown in Figure 16a and 16b, respectively. Both methods can image the sources in the complex fault model. Because the reflection interfaces of the fault act as secondary sources, they can also be imaged by using time-reverse imaging, which affects the location resolution and generates false images. The WEW interferometric imaging method is not affected by the surrounding reflection interfaces. The imaging amplitude and resolution of the location of both methods decreases

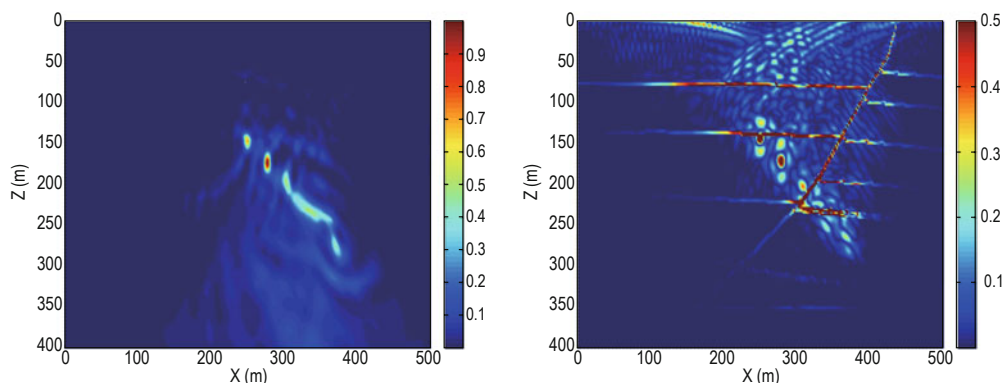


Fig.16 Profile of the weighted-elastic-wave interferometric imaging (a) and time-reverse imaging (b).

Microseismic source location

as the source–receiver distance increases, especially the location errors of the two sources in the low-velocity zone is relatively large.

Second, we simulate five continuously excited

sources with equal amplitudes. The locations of the simultaneously and continuously excited sources of both methods are shown in Figure 17.

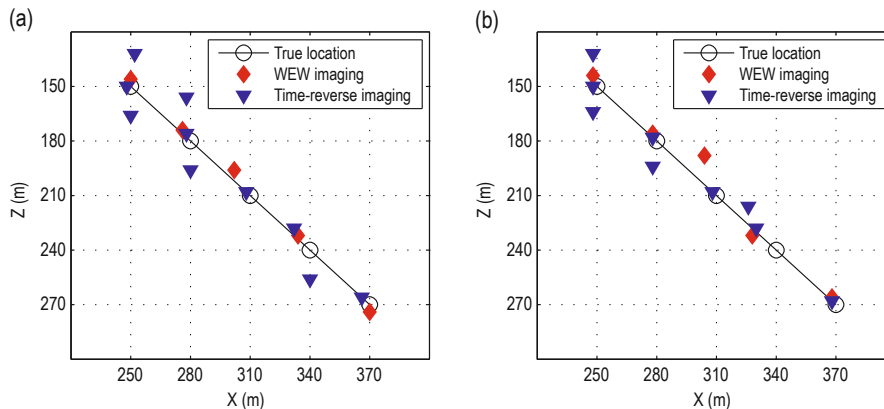


Fig.17 Location of the five simultaneously excited (a) and continuously excited sources (b).

Figure 17 shows that both methods can locate sources in the complex fault model accurately. The maximum location error is within 20 m. Time-reverse imaging produces several false images near the reflection interfaces and the weighted-elastic-wave interferometric imaging has higher location precision.

Conclusions

Elastic wave interferometric imaging is applied to multiwavefield and multicomponent microseismic data to locate the source. The weighted-elastic-wave interferometric imaging method is also introduced. We assume a horizontally layered isotropic medium and use numerical experiments to test the stability and reliability of the method. The method does not require prior knowledge of the excitation time, the first arrival time, or separate wavefields. Therefore, the method shows high calculation efficiency. The traveltimes differences of individual wavefields from different sources are independent; thus, the weighted-elastic-wave interferometric imaging method may be used to locate multiple sources with higher precision and efficiency compared with time-reverse imaging.

References

Anikiev, D., Valenta, J., Staněk, F., and Eisner, L., 2014,

Joint location and source mechanism inversion of microseismic events: Benchmarking on seismicity induced by hydraulic fracturing: *Geophysical Journal International*, **198**(1), 249–258.

Artman, B., Podladtchikov, I., and Witten, B., 2010, Source location using time-reverse imaging: *Geophysical Prospecting*, **58**, 861–873.

Bardainne, T., Gaucher, E., Magnitude, and Cerda, F., 2009, Comparison of picking-based and waveform-based location methods of microseismic events: Application to a fracturing job: *79th Ann. Soc. Expl. Geophys. Mtg., Expanded Abstracts*, 1547–1551.

Burch, D. N., Daniels, J., Gillard, M., Underhill, W., Exler, V. A., Favoretti, L., Le Calvez, J., Lecerf, B., Potapenko, D., and Maschio, L., 2009, Live hydraulic fracture monitoring and diversion: *Oilfield Review*, **21**(3), 18–31.

Chambers, K., Dando, B. D. E., Jones, G. A., Velasco, R., and Wilson, S. A., 2014, Moment tensor migration imaging: *Geophysical Prospecting*, **62**(4), 879–896.

Claerbout, J. F., 1968, Synthesis of a layered medium from its acoustic transmission response: *Geophysics*, **33**(2), 264–269.

Das, I., and Zoback, M., 2013, Long-period, long-duration seismic events during hydraulic stimulation of shale and tight-gas reservoirs - part 1: Waveform characteristics: *Geophysics*, **78**(6), KS97–KS108.

Dong, L. G., Ma, Z. T., Cao, J. Z., Wang, H. Z., Geng, J. H., Lei, B., and Xu, S. Y., 2000, A staggered-grid high-order difference method of one-order elastic wave equation: *Chinese Journal of Geophysics (in Chinese)*, **43**(3), 411–419.

Drew, J. E., Leslie, H. D., Armstrong, P. N., and Michard,

- G., 2005, Automated microseismic event detection and location by continuous spatial mapping: The 81st SPE Annual Technical Conference and Exhibition, SPE Paper 95513.
- Drew, J. E., White, R. S., Tilmann, F., and Tarasewicz, J., 2013, Coalescence microseismic mapping: *Geophysical Journal International*, **195**(3), 1773–1785.
- Duncan, P. M., and Eisner, L., 2010, Reservoir characterization using surface microseismic monitoring: *Geophysics*, **75**(5), 75A139–175A146.
- Eisner, L., Hulsey, B. J., Duncan, P., Jurick, D., Werner, H., and Keller, W., 2010, Comparison of surface and borehole locations of induced seismicity: *Geophysical Prospecting*, **58**(5), 809–820.
- Fink, M., 1999, Time-reversed acoustics: *Scientific American*, November, 91–97.
- Gajewski, D., and Tessmer, E., 2005, Reverse modelling for seismic event characterization: *Geophysical Journal International*, **163**(1), 276–284.
- Gajewski, D., Anikiev, D., Kashtan, B., and Tessmer, E., 2007, Localization of seismic events by diffraction stacking: 77th Ann. Soc. Expl. Geophys. Mtg., Expanded Abstracts, 1287–1291.
- Geiger, L., 1912, Probability method for the determination of earthquake epicenters from arrival time only: *Bull St Louis Univ*, **8**, 60–71.
- Gharti, H. N., Oye, V., Kühn, D., and Zhao, P., 2011, Simultaneous microearthquake location and moment-tensor estimation using time-reversal imaging: 81st Ann. Soc. Expl. Geophys. Mtg., Expanded Abstracts, 1632–1637.
- Grandi, S., and Oates, S., 2009, Microseismic event location by cross-correlation migration of surface array data for permanent reservoir monitoring: 71st Conference & Technical Exhibition, EAGE, Extended Abstracts, X012.
- Grigoli, F., Cesca, S., Vassallo, M., and Dahm, T., 2013, Automated seismic event location by travel - time stacking: An application to mining induced seismicity: *Seismological Research Letters*, **84**(4), 666–677.
- Grigoli, F., Cesca, S., Amoroso, O., Emolo, A., Zollo, A., and Dahm, T., 2014, Automated seismic event location by waveform coherence analysis: *Geophysical Journal International*, **196**(3), 1742–1753.
- Haldorsen, J. B. U., Milenkovic, M., Farmani, M. B., Brooks, N., and Crowell, C., 2012, Locating microseismic events using migration-based deconvolution: 82nd Ann. Soc. Expl. Geophys. Mtg., Expanded Abstracts, 1–5.
- Haldorsen, J. B. U., Brooks, N. J., and Milenkovic, M., 2013, Locating microseismic sources using migration-based deconvolution: *Geophysics*, **78**(5), KS73–KS84.
- Jupe, A., Cowles, J., and Jones, R., 1998, Microseismic monitoring: Listen and see the reservoir: *World Oil*, **219**(12), 171–174.
- Kao, H., and Shan, S. J., 2004, The source-scanning algorithm: Mapping the distribution of seismic sources in time and space: *Geophysical Journal International*, **157**(2), 589–594.
- Kao, H., and Shan, S. J., 2007, Rapid identification of earthquake rupture plane using source-scanning algorithm: *Geophysical Journal International*, **168**(3), 1011–1020.
- Li, J. L., Zhang, H. J., Rodi, W. L., and Toksoz, M. N., 2013, Joint microseismic location and anisotropic tomography using differential arrival times and differential backazimuths: *Geophysical Journal International*, **195**(3), 1917–1931.
- Li, Z. C., Sheng, G. C., Wang, W. B., Cui, Q. H., and Zhou, D. S., 2014, Time-reverse microseismic hypocenter location with interferometric imaging condition based on surface and downhole multi-components: *Oil Geophysical Prospecting*, **49**(4), 661–666, 671.
- Liang, B., and Zhu, G. S., 2004, *Microseismic monitoring in oil and gas field exploration and development*: Petroleum Industry Press, Beijing.
- Maxwell, S. C., 2010a, Microseismic: Growth born from success: *The Leading Edge*, **29**, 338–343.
- Maxwell, S. C., Rutledge, J., Jones, R., and Fehler, M., 2010b, Petroleum reservoir characterization using downhole microseismic monitoring: *Geophysics*, **75**(5), 75A129–175A137.
- McMechan, G. A., 1982, Determination of source parameters by wavefield extrapolation: *Geophysical Journal International*, **71**(4), 613–628.
- McMechan, G. A., H. Luetgert, J., and Mooney, W. D., 1985, Imaging of earthquake sources in long valley caldera, California, 1983: *Bulletin of the Seismological Society of America*, **75**, 1005–1020.
- Miao, H. X., Jiang, F. X., Song, X. J., Song, J. Y., Yang, S. H., and Jiao, J. R., 2012a, Automatically positioning microseismic sources in mining by the stereo tomographic method using full wavefields: *Applied Geophysics*, **9**(2), 168–176.
- Miao, H. X., Jiang, F. X., Song, X. J., Yang, S. H., and Jiao, J. R., 2012b, Tomographic inversion for microseismic source function and parameters in mining: *Applied Geophysics*, **9**(3), 341–348.
- Mueller, M., 2013, Meeting the challenge of uncertainty in surface microseismic monitoring: *First Break*, **31**(7), 89–95.
- Schuster, G. T., 2001, *Theory of daylight/interferometric imaging: Tutorial*: 63rd Conference & Technical Exhibition, EAGE, Expanded Abstracts, A32.

Microseismic source location

- Schuster, G. T., 2009, *Seismic interferometry*: Cambridge University Press Cambridge, New York.
- Schuster, G. T., Yu, J., and Sheng, J., 2004, Interferometric/daylight seismic imaging: *Geophysical Journal International*, **157**(2), 838–852.
- Song, W. Q., Chen, Z. D., and Mao, Z. H., 2008, *Hydrofracturing break microseismic monitoring technology*: China University of Petroleum Press, Dongying.
- Tian, Y., and Chen, X. F., 2002, Review of seismic location study: *Progress in Geophysics*, **17**(1), 147–155.
- Wang, C. L., Cheng, J. B., Yin, C., and Liu, H., 2013, Microseismic events location of surface and borehole observation with reverse-time focusing using interferometry technique: *Chinese Journal of Geophysics (in Chinese)*, **56**(9), 3184–3196.
- Wapenaar, K., Draganov, D., and Snieder, R., 2010a, Tutorial on seismic interferometry: Part 1 — basic principles and applications: *Geophysics*, **75**(5), 75A195–175A209.
- Wapenaar, K., Slob, E., and Snieder, R., 2010b, Tutorial on seismic interferometry: Part 2—underlying theory and new advances: *Geophysics*, **75**(5), 75A211–275A227.
- Xiao, X., Luo, Y., Fu, Q., Jervis, M., Dasgupta, S., and Kelamis, P., 2009, Locate microseismicity by seismic interferometry: EAGE Passive Seismic Workshop, Extended Abstract, A22.
- Yang, R. Z., Zhao, Z. G., Peng, W. J., Gu, Y. B., Wang, Z. G., and Zhuang, X. Q., 2013, Integrated application of 3d seismic and microseismic data in the development of tight gas reservoirs: *Applied Geophysics*, **10**(2), 157–169.
- Yang, W. D., Jin, X., Li, S. Y., and Ma, Q., 2005, Study of seismic location methods: *Earthquake Engineering and Engineering Vibration*, **25**(1), 14–20.
- Yilmaz, Ö., 2001, *Seismic Data Analysis: Processing, Inversion and Interpretation of Seismic Data*: Society of Exploration Geophysicists.
- Zhang, S., Liu, Q. L., Zhao, Q., and Jiang, Y. D., 2002, Application of microseismic monitoring technology in development of oil field: *Geophysical Prospecting for Petroleum (in Chinese)*, **41**(2), 226–231.
- Zhebel, O., and Eisner, L., 2012, Simultaneous microseismic event localization and source mechanism determination: 82nd Ann. Soc. Expl. Geophys. Mtg., Expanded Abstracts, 1–5.
- Zhebel, O., Gajewski, D., and Vanelle, C., 2010, Localization of seismic events in 3d media by diffraction stacking: 80th Ann. Soc. Expl. Geophys. Mtg., Expanded Abstracts, 2181–2185.

Li Lei, PhD student, Institute of Acoustics, Chinese Academy of Sciences. Main research interests are seismic wave propagation and microseismic event location and imaging.

